Nano Research 2018, 11(12): 6227–6236
https://doi.org/10.1007/s12274-018-2142-5
Research Article
ISSN 1998-0124
CN 11-5974/O4

Intrinsic excitonic emission and valley Zeeman splitting in epitaxial MS_2 (M = Mo and W) monolayers on hexagonal boron nitride

Chunxiao Cong[1,§] (✉), Chenji Zou[2,§], Bingchen Cao[2,§], Lishu Wu[2], Jingzhi Shang[2] (✉), Haomin Wang[3], Zhijun Qiu[1] (✉), Laigui Hu[1], Pengfei Tian[1], Ran Liu[1], and Ting Yu[2] (✉)

[1] *State Key Laboratory of ASIC and System, School of Information Science and Technology, Fudan University, Shanghai 200433, China*
[2] *Division of Physics and Applied Physics, School of Physical and Mathematical Sciences, Nanyang Technological University, Singapore 637371, Singapore*
[3] *State Key Laboratory of Functional Materials for Informatics, Shanghai Institute of Microsystem and Information Technology, Chinese Academy of Sciences, 865 Changning Road, Shanghai 200050, China*
[§] *Chunxiao Cong, Chenji Zou, and Bingchen Cao contributed equally to this work.*

Received: 20 May 2018
Revised: 23 June 2018
Accepted: 2 July 2018

KEYWORDS
transition metal dichalcogenides, intrinsic excitonic emission, valley Zeeman splitting, hexagonal boron nitride, chemical vapor deposition

ABSTRACT

Two-dimensional (2D) semiconductors, represented by 2D transition metal dichalcogenides (TMDs), exhibit rich valley physics due to strong spin-orbit/spin-valley coupling. The most common way to probe such 2D systems is to utilize optical methods, which can monitor light emissions from various excitonic states and further help in understanding the physics behind such phenomena. Therefore, 2D TMDs with good optical quality are in great demand. Here, we report a method to directly grow epitaxial WS_2 and MoS_2 monolayers on hexagonal boron nitride (hBN) flakes with a high yield and high optical quality; these monolayers show better intrinsic light emission features than exfoliated monolayers from natural crystals. For the first time, the valley Zeeman splitting of WS_2 and MoS_2 monolayers on hBN has been visualized and systematically investigated. This study paves a new way to produce high optical quality WS_2 and MoS_2 monolayers and to exploit their intrinsic properties in a multitude of applications.

1 Introduction

Two-dimensional (2D) transition metal dichalcogenides (TMDs) of 2H structure, such as WS_2, MoS_2, WSe_2, and $MoSe_2$, are considered to be emerging semiconductors not only because they possess a direct energy-band

Address correspondence to Chunxiao Cong, cxcong@fudan.edu.cn; Zhijun Qiu, zjqiu@fudan.edu.cn; Jingzhi Shang, JZShang@ntu.edu.sg; Ting Yu, yuting@ntu.edu.sg

gap, but also own an extra valley degree of freedom. A direct energy-band gap in the visible light range, strong spin-orbit/spin-valley coupling, and the newly discovered ferromagnetism of 2D materials offer rich new physical aspects and promise plenty of applications, such as 2D light emission diodes (LEDs), 2D lasers, 2D valleytronics, and others [1–14].

Chemical vapor deposition (CVD) is believed to be the most suitable method to produce 2D materials for intensive fundamental studies and practical applications. Currently, the most common method to grow atomic-level thin layers of TMDs via CVD is to react metal oxide powders with sulfur or selenium vapors. This method works fairly well for the substrates of SiO_2/Si, quartz, sapphire, mica, and Au foils, which have been extensively investigated [15–23]. Meanwhile, it is known that hexagonal boron nitride (hBN) is the most desirable substrate for growing or transferring 2D materials, as it provides a clean, flat, and neutral surface/interface to 2D materials, which guarantees high crystal or optical quality in 2D TMDs and induces 2D TMDs to exhibit their intrinsic properties [24–32]. Unfortunately, thus far, there have been very few reports on growing TMDs monolayers on hBN substrates using CVD [25, 33–35] or using WCl_6 and sulfur [24]. Though CVD-grown WS_2 and MoS_2 monolayers on hBN show much better optical quality compared to CVD-grown or mechanically exfoliated WS_2 and MoS_2 monolayers on SiO_2/Si substrates [24, 25, 34, 35], systematic studies on their properties, such as their optical and spin-valley properties, are lacking; this may be attributed to their small size and low production [24, 34].

Typically, monolayers of TMDs prepared by mechanical exfoliation of natural crystals are used when research is focused on exploiting the intrinsic properties and fundamental mechanism of 2D TMDs. Indeed, exfoliated WSe_2 and $MoSe_2$ monolayers on SiO_2/Si exhibit excellent optical quality, such as well-resolved and sharp exciton (X_0) and trion (X_T) emission peaks [36–41]. This is the main reason for choosing Se-based 2D TMDs for studies on valley physics in 2D semiconductors, such as valley splitting, one of the most interesting valley physical aspects of 2D TMDs [36–39]. However, in the case of S-based TMDs, such as WS_2 and MoS_2, the exfoliated monolayers on SiO_2/Si, in spite of a certain improvement in the optical quality when compared to CVD-grown monolayers of WS_2 and MoS_2 on SiO_2/Si, exhibit a broad peak of highly merged exciton and trion emissions at room temperature or very weak and broadly separated exciton and trion emissions with strong emissions of localized states even at cryogenic temperatures [26, 42–44]. Such poor optical quality greatly limits investigation on their intrinsic light emission properties and physics. Recently, Cadiz et al. observed very narrow optical transition linewidths in MoS_2 and WS_2 monolayers encapsulated in hBN [26]. However, the encapsulation process is complicated and not suitable for large-area and high-yield production.

In this study, we developed a method for directly growing WS_2 and MoS_2 atomic-level thin layers on hBN substrates using CVD. The as-grown triangular WS_2 and MoS_2 monolayer flakes cover almost the entire hBN surface and align themselves according to a certain orientation, which suggests a high yield for the epitaxial-growth process. Compared to the monolayers exfoliated from natural crystals on SiO_2/Si, our CVD monolayers on hBN exhibit a significantly improved optical quality with neutral exciton linewidths of ~ 5.6 and ~ 7.2 meV at cryogenic temperature for MoS_2 and WS_2, respectively. Intrinsic excitonic emissions, such as well-resolved and super sharp exciton and trion photoluminescence (PL) peaks, could be observed. The intrinsic valley Zeeman splitting in CVD-grown WS_2 and MoS_2 monolayers on hBN could be clearly observed by *in-situ* magnetic-field-dependent PL imaging and spectroscopy at cryogenic temperature; such a systematic study is being conducted for the first time.

2 Results and discussion

Though our previously developed method could be successfully used to grow large-area WS_2 monolayers on SiO_2/Si [17], it is not so successful in growing WS_2 monolayer flakes directly on hBN. As shown in Fig. S1 in the Electronic Supplementary Material (ESM), when WO_3 powders are used as the precursor, WS_2 layers prefer to nucleate at the edges of hBN flakes and grow laterally like extensions instead of growing on top of the basal plane of hBN. The strategy

designed in this study is to provide transition-metal sources by precoating hBN flakes and the exposed area of SiO_2/Si with a uniform thin film of WO_x. The subsequent sulfurization process promotes the growth of WS_2 atomic-level thin flakes directly on top of hBN (Fig. 1(a)). While the refractive index and thickness of the hBN flake do not offer an acceptable optical contrast of WS_2 monolayers on hBN (Fig. 1(b)), the scanning electron microscope (SEM) image does display the expected result; it indicates a large population of atomic-level thin WS_2 flakes on the entire surface of hBN, which indicates the high yield of this new method (Fig. 1(c)). The bright fluorescence emission further reveals that the majority of the products are monolayer flakes (Fig. 1(d) and Fig. S2 in the ESM), which possess a direct band gap. The triangular shape of the as-grown WS_2 flakes is deciphered by atomic force microscopy (AFM) and the height profile confirms the formation of the monolayers (Fig. 1(e)). A perfect alignment of crystal orientations among the as-grown flakes could be observed in the AFM image, implying the epitaxial growth of WS_2 monolayers on hBN. High yield and epitaxial growth occur on almost all pieces of hBN (Fig. S3 in the ESM) and the statistic size distribution histogram of as-grown WS_2 can be found in Fig. S4 in the ESM. A typical Raman spectrum of monolayer WS_2 grown on hBN is displayed in Fig. 1(f). The $E^1_{2g}(\Gamma)$ peak at 355 cm^{-1} originates from atomic in-plane vibrations, while the $A_{1g}(\Gamma)$ mode at 417 cm^{-1} originates from the out-of-plane vibration of the atoms. In addition to the $E^1_{2g}(\Gamma)$ and $A_{1g}(\Gamma)$ modes, the peak at ~ 300 cm^{-1} is attributed to $2LA(M)-2E^2_{2g}(\Gamma)$, the peak at ~ 320 cm^{-1} is attributed to $2LA(M)-E^2_{2g}(\Gamma)$, and the peak at ~ 350 cm^{-1} is attributed to $2LA(M)$, where LA(M) is a longitudinal acoustic mode caused by in-plane collective movements of atoms [17, 45].

The PL spectra of monolayer WS_2 grown on hBN and the WS_2 mechanically exfoliated monolayer on SiO_2/Si are shown in Fig. 1(g). Interestingly, the WS_2 monolayer directly grown on hBN by CVD exhibits a much sharper PL peak (linewidth of 29 meV), compared to monolayer WS_2 on SiO_2/Si fabricated by the mechanical exfoliation of a natural crystal (linewidth of 80 meV). An obvious blue shift of the PL peak could also be noticed in the CVD-grown monolayer,

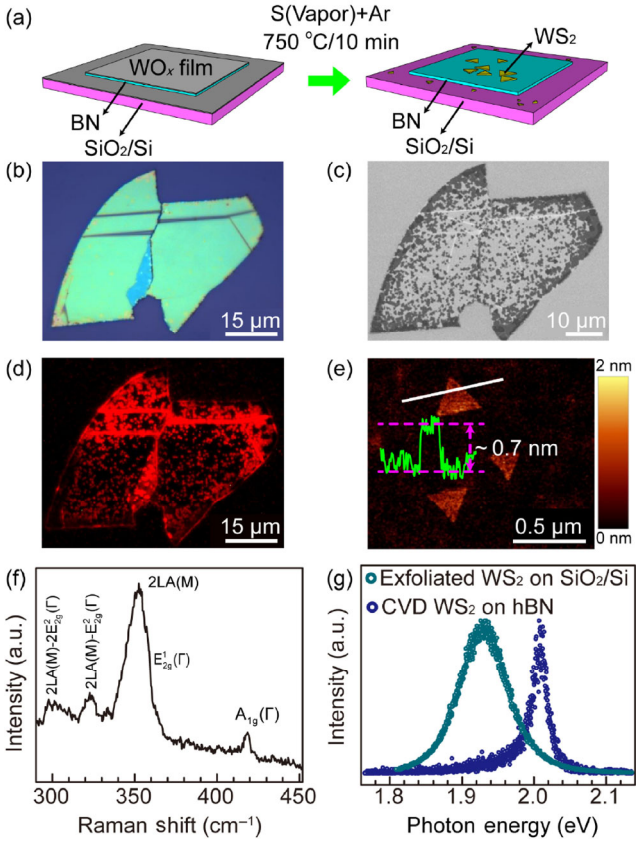

Figure 1 (a) Schematic diagram of the growth of WS_2 monolayer flakes on hBN. (b)–(d) Optical, SEM, and fluorescence images of WS_2 atomic-level thin layers grown on hBN. (e) AFM image of WS_2 monolayers. The inset shows the height profile across the selected flake. (f) Raman spectrum of monolayer WS_2 grown on hBN. (g) PL spectra of monolayer WS_2 grown on hBN and mechanically exfoliated monolayer WS_2 on SiO_2/Si. The measurements were conducted at room temperature.

compared to the case of the monolayer exfoliated on SiO_2/Si, which is probably due to the Coulomb screening difference, strain, and lesser electrical perturbation experienced by the monolayer grown on hBN [27, 34, 46, 47]. Such remarkable sharpening and hardening of the PL peak of the CVD-grown monolayer WS_2 on hBN can be ascribed to the significant improvement in the sample's crystal and optical quality, which in turn are a result of suppressing the unintentional doping by the oxide substrate. This is a known and widely adapted advantage of hBN substrates. It is also noticed that the monolayers prepared by this method are chemically robust. Their good PL features could be maintained even after the samples were stored in ambient conditions for more than a year. The observed feature of a narrow intrinsic exciton emission

peak promises more opportunities for investigating WS_2 monolayers.

To further probe the intrinsic excitonic emissions from epitaxial WS_2 monolayer flakes on hBN substrates, PL microscopy and mapping were conducted at cryogenic temperature. For comparison, light emission from WS_2 monolayers exfoliated from natural crystals was also measured. In the case of the exfoliated sample, though the neutral exciton and charged trion emissions could be resolved, for example, by careful curve fitting, the two emission features merge heavily with each other and with a bunch of localized emissions (Fig. 2(a) top). In contrast, the exciton and trion emissions of the CVD-grown monolayer WS_2 on hBN are well separated and their linewidths are only ~ 7 and ~ 10 meV, respectively (Fig. 2(a) bottom). Figures 2(b) and 2(c) show the PL mapping of the CVD grown monolayer WS_2 on hBN, extracted from the integrated intensity and energy of the neutral exciton emission. The intrinsic exciton and trion emission energies and the trion associate energy are 2.083, 2.046 eV, and 37 meV, respectively, which agree well with the reported theoretical and experimental values [48–52]. Usually, exfoliated samples from a natural crystal are believed to be of high quality and uniformity. In fact, we notice that non-uniformities, such as the exciton emission energy, exist in the exfoliated WS_2 monolayer on SiO_2/Si (Fig. S5 in the ESM). Taking advantage of the well-resolved intrinsic excitonic emissions of our CVD-grown WS_2 monolayer flakes on hBN, to visualize such intrinsic emissions from different flakes, we performed PL mapping in a selected area (Fig. S6 in the ESM) at cryogenic temperature. As flake dimensions are beyond the resolution of our system, individual triangular flakes could not be resolved properly. Non-uniformity of exciton emission strength as well as energy could be observed in the scanning area.

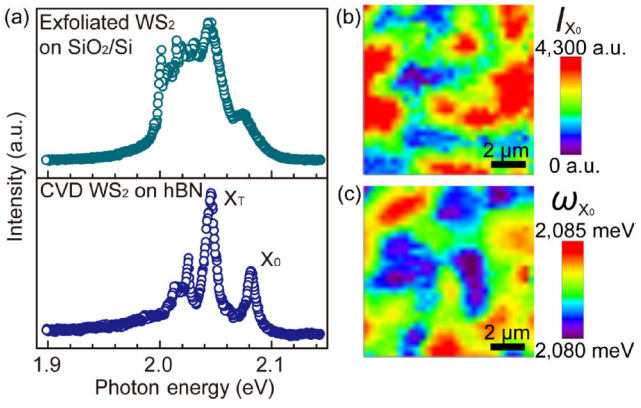

Figure 2 (a) PL spectrum of a mechanically exfoliated WS_2 monolayer on a SiO_2/Si substrate (top) and PL spectrum of a CVD-grown WS_2 monolayer on hBN (bottom). (b) PL mapping extracted from the integrated intensity of neutral exciton emission. (c) PL mapping extracted from the energy of neutral-exciton emission. The measurements were conducted at 4.2 K.

Because the exciton and trion emissions from CVD-grown WS_2 monolayer flakes on hBN are well-resolved and intrinsic, we were able to probe the physical phenomena responsible for such light emissions from excitonic states. Here, our focus is to visualize magnetic field-tuned valley splitting. Figure 3 presents the PL images of the exciton (X_0) and trion (X_T) emission energies at select magnetic fields. At zero field, though both exciton and trion emissions exhibit different energies across the mapping area, a good correspondence could be observed between the PL images of the exciton (X_0) (Figs. 3(a1) and 3(b1)) and trion (X_T) (Figs. 3(a2) and 3(b2)) emission energies at the *K′* and *K* valleys, indicating the degeneracy of the exciton and trion states. A remarkable contrast appears in both exciton and trion emission energy mappings when a high magnetic field is applied (±8 T). At a magnetic field strength of +8 T, both the exciton and trion emission energies at the *K′* valley are higher than those at the *K* valley. Such contrast is totally opposite to the situation at a magnetic field of –8 T. The energy difference between light emissions from the exciton and trion excitonic states at the two valleys at a given magnetic field indicates the breaking of valley degeneracy or alternatively the occurrence of valley Zeeman splitting, which is induced by the net magnetic moment of W orbital angular momentum in the valence band when subject to an out-of-plane external magnetic field [36–39]. Similar observations have been reported for $MoSe_2$ and WSe_2, which show well-resolved and intrinsic PL peaks through magnetic-field-dependent PL measurement [36–39], but rarely in WS_2 nor MoS_2 due to its poor light-emission features, such as its overly broad and merged PL peaks. To comprehensively understand magnetic field-tuned evolution of excitonic states in the two valleys and to visualize such valley splitting in different pieces of

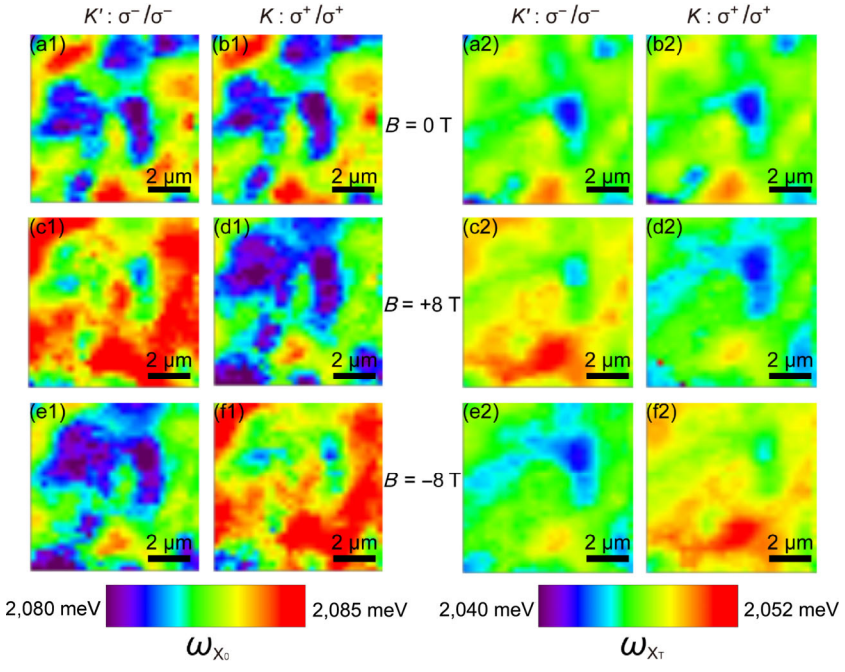

Figure 3 (a1)–(f1) PL images of the exciton (X_0) emission energies at magnetic fields of 0 T, +8 T, and –8 T with σ^+ and σ^- polarizations. (a2)–(f2) PL images of the trion (X_T) emission energies at magnetic fields of 0 T, +8 T, and –8 T with σ^+ and σ^- polarizations. The measurements were conducted at 4.2 K.

as-grown WS_2 monolayer flakes on hBN, we carried out *in-situ* magnetic-field-dependent PL mapping by swiping the magnetic field strength from +8 to –8 T (Figs. S7 and S8 in the ESM). With an increase in the field strength in the positive direction, exciton and trion emissions from the *K′* valley gradually increased, while the energies of exciton and trion emissions from the *K* valley decreased. The opposite trend was observed when a negatively increasing magnetic field was applied.

Though different light-emission energies are encountered across the scanning area, the evolution of valley splitting seems to be consistent locally. To further exploit this hypothesis and reveal the intrinsic magnetic-field dependency of valley Zeeman splitting in CVD-grown WS_2 monolayers on hBN, we selected three individual areas exhibiting uniform light emission energies to conduct statistical analysis (Fig. S9 in the ESM) and extract the averaged PL spectra from the selected three individual regions as typical spectra. The relative shifts of exciton and trion emission peaks in a strong magnetic field display and represent the differences in the energy gaps of corresponding excitonic states in the two valleys (Fig. 4(a)). The valley Zeeman splitting energy as a function of magnetic field strength fits into a perfect straight-line shape (Fig. 4(b)). The extracted slopes are –0.22 and –0.29 meV/T for the exciton and trion, respectively. The intrinsic *g*-factors of the CVD-grown WS_2 monolayer flakes on hBN are 3.85 for the exciton and 5.04 for the trion, which agree well with theoretical predictions and are very close to the experimental observations on WSe_2 and $MoSe_2$ [36–39]. The slopes and *g*-factors of the exciton and

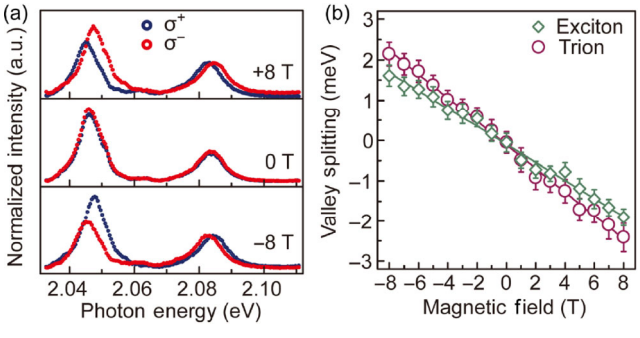

Figure 4 (a) Typical PL spectra (X_0 and X_T emissions after removing the background) of CVD-grown monolayer WS_2 on hBN at different magnetic field strengths from the selected area 1 (see Fig. S9 in the ESM). (b) The measured valley Zeeman splitting as a function of the magnetic field corresponding to the exciton (X_0) and trion (X_T). The measurements were conducted at 4.2 K.

trion for other two areas indeed consist with each other (Fig. S10 in the ESM).

Further, we extended our strategy to grow MoS_2 monolayers on hBN. MoS_2 monolayers are one of the most widely studied 2D TMDs. Unfortunately, the optical quality of CVD-grown MoS_2 monolayers, even the exfoliated ones, is not as good as that of $MoSe_2$ or WSe_2. A broad peak consisting of an unresolvable exciton and trion is typically observed in the PL spectrum of monolayer MoS_2 even at low temperatures [44], which hinders the study of its intrinsic emission properties and new physical aspects. It is obvious that the newly developed method proposed in this study works well for achieving high yields of atomic-level thin MoS_2 flakes on hBN (Figs. 5(a) and 5(b)). The triangular shape, epitaxial growth, and monolayer products are clearly featured in the magnified SEM image, AFM image, and Raman spectra (Fig. S11 in the ESM). A statistical size-distribution histogram of as-grown MoS_2 can be found in Fig. S12 in the ESM. Similar to WS_2, excitonic light emissions from CVD-grown monolayer MoS_2 flakes on hBN exhibit a blue shift and are narrower when compared to those of the mechanically exfoliated sample from natural crystals (Fig. 5(c)), which suggests an improved optical quality for the CVD-grown MoS_2 monolayers on hBN. The PL image extracted from the integrated intensity of the dominant peak at 1.88 eV for the CVD-grown MoS_2 flakes on hBN further demonstrates the high yield achieved through this method (Fig. 5(d)).

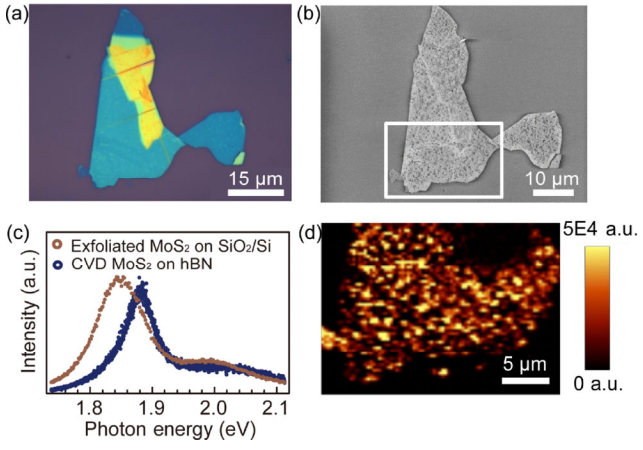

Figure 5 (a) and (b) Optical and SEM images of atomic-level thin MoS_2 flakes grown on hBN. (c) PL spectra of CVD-grown MoS_2 monolayer flakes on hBN and exfoliated MoS_2 monolayers on SiO_2/Si. (d) PL image of the MoS_2 flakes on hBN developed by extracting the integrated intensity of the intense peak at 1.88 eV. The frame in (b) shows the PL mapping area. The measurements were conducted at room temperature.

Cooling a semiconductor to cryogenic temperatures is commonly carried out to suppress the influence of thermal fluctuations and uncover its natural properties. Here, we performed *in-situ* low-temperature (4.2 K) PL spectroscopy and imaging studies on the as-grown MoS_2 monolayer flakes on hBN. A dramatically sharp peak appeared at 1.96 eV with a linewidth of 5.6 meV, which is much narrower than that of the exfoliated sample on SiO_2/Si (Fig. 6(a)). To the best of our knowledge, this is the narrowest PL peak reported for CVD-grown MoS_2 monolayers. Such a sharp PL peak is believed to represent intrinsic light emission from the neutral exciton of MoS_2 monolayers. The well-resolved and super-narrow exciton emission peak observed with our CVD-grown MoS_2 monolayer flakes on hBN offers great possibilities towards comprehending valley physics phenomena, such as valley splitting, in such 2D direct-bandgap semiconductors. By mapping the selected area (Fig. 5(b)) at cryogenic temperature and extracting the exciton emission energies from the K' and K valleys at different magnetic fields (Fig. 6(b) and Fig. S13 in the ESM), we demonstrated the degeneracy of the excitonic states between the two valleys when there was no magnetic field and the lifting-up of such degeneracy under the action of a strong magnetic field in CVD-grown monolayer MoS_2 flakes on hBN. Such magnetic-field induced valley splitting is also reflected by the shifts in the exciton emission peaks, as shown in Fig. 6(c). The valley Zeeman splitting energy of the neutral exciton as a function of magnetic field strength is shown in Fig. 6(d). The extracted slope is –0.079 meV/T. The g-factor of CVD-grown MoS_2 monolayer flakes on hBN was determined to be 1.36, which is smaller than that of WS_2 and Se-based 2D TMDs [36–39] and might be due to the intrinsic properties of MoS_2 [26]. Further studies on these aspects are ongoing.

3 Conclusions

In summary, a method for directly growing WS_2 and MoS_2 monolayer flakes on hBN substrates at a high yield has been successfully developed. The obtained

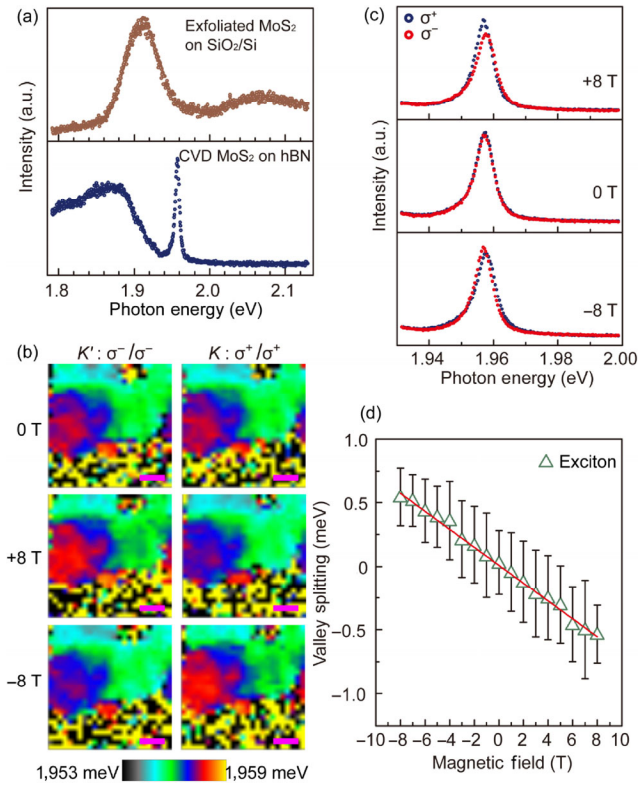

Figure 6 (a) PL spectrum of a mechanically exfoliated MoS_2 monolayer on a SiO_2/Si substrate (top) and PL spectrum of CVD-grown MoS_2 monolayer flakes on hBN (bottom). (b) PL images of the exciton (X_0) emission energies at different magnetic fields with σ^+ and σ^- polarizations. Scale bar: 5 μm. (c) Typical PL spectra (X_0) of monolayer MoS_2 at different magnetic fields with σ^+ and σ^- polarizations. (d) The measured valley Zeeman splitting as a function of the magnetic field for the exciton (X_0). The measurements were conducted at 4.2 K.

as-grown monolayer flakes exhibited a high optical quality. By further optimizing the material and process recipe for this growth method, not only high-optical quality and high-yield but also large-size monolayer MS_2 (M = Mo and W) can be obtained, which is beneficial for future electronic or valleytronic applications; such methods can obviate additional sample-transfer processes. The intrinsic exciton and trion emissions of these monolayers were studied by probing their well-resolved and sharp PL peaks. Magnetic-field-dependent PL mapping was used to visualize valley Zeeman splitting in WS_2 and MoS_2 monolayer flakes grown on hBN. The intrinsic *g*-factors of these two promising 2D semiconductors were determined. This study paves a new way to produce WS_2 and MoS_2 monolayers of high optical quality and further exploit new physical features and applications connected with such interesting 2D systems.

4 Experimental

4.1 Sample preparation

WS_2 and MoS_2 atomic-level thin flakes were grown using a chemical vapor deposition process in a tube-furnace system we developed previously [17]. Instead of metal oxide powders, metal oxide (WO_x and MoO_x) thin films (1-nm thick) were deposited onto the pre-exfoliated hBN flakes on a SiO_2/Si substrate by e-beam evaporation. Pure Ar gas at a flow rate of 100 sccm was used as the carrying gas. The growth temperature was controlled at 750 ˚C, while the growth duration was set to 10 min. The reference samples, mechanically exfoliated WS_2 and MoS_2 monolayers, were made from natural crystals (purchased from 2D semiconductors Inc.) and transferred onto typical SiO_2/Si substrates.

4.2 Characterization of the as-grown samples at room temperature

The as-grown samples were firstly characterized at room temperature. Their optical and fluorescence images were recorded using an optical microscope (Olympus BX51) equipped with a Mercury lamp. A scanning electron microscope (JEOL JSM-6700F) and an atomic force microscope (WITec alpha 300 RA with AFM function) were employed for the morphological studies of WS_2 and MoS_2 atomic-level thin flakes on hBN. Raman and photoluminescence spectroscopic studies were conducted using a WITec alpha 300 RAS Raman/PL system with an excitation laser of 532 nm and a 100X objective lens of 0.95 numerical aperture (NA). To avoid the effects of heating, the laser power was controlled below 0.1 mW. The laser spot size was around 500 nm in diameter. A 2,400 lines/mm grating and a 600 lines/mm grating were used for Raman and PL measurements, respectively.

4.3 PL spectroscopy and imaging studies of the monolayer flakes at cryogenic temperature

The as-grown WS_2 and MoS_2 monolayer flakes on hBN were also analyzed at cryogenic temperature

(4.2 K) using a custom-designed confocal micro-PL spectroscopy/image system with a non-magnetic piezo-crystal-controlled sample stage consisting of *x*-, *y*-, and *z*- axis positioners and *x*- and *y*- axis scanners. The excitation source was a continuous-wave laser of 532 nm with a power of ~ 0.3 mW. The laser spot size was estimated to be ~ 1 μm in diameter. A 600 lines/mm grating was used for PL measurements. Magnetic fields in the range of +8 T to –8 T were applied perpendicular to the plane of the as-grown WS_2 and MoS_2 monolayers. Light emission from either the *K′* valley or the *K* valley was selectively probed by controlling the circular polarization states of the incident and scattering lights.

Acknowledgements

This work is supported by the National Natural Science Foundation of China (Nos. 61774040, 11774170, and 61774042), the Opening project of State Key Laboratory of Functional Materials for Informatics (Shanghai Institute of Microsystem and Information Technology, Chinese Academy of Sciences), the National Young 1000 Talent Plan of China, the Shanghai Municipal Natural Science Foundation (Nos. 16ZR1402500, 17ZR1446500, and 17ZR1446600), NTU Start-up grant M4080513, Singapore Ministry of Education (MOE) Tier 1 RG199/17, and Shanghai Pujiang Program (No. 16PJ1401000). C. C. thanks Dr. Ute Schmidt from WITec Company for AFM measurement.

Electronic Supplementary Material: Supplementary material (statistic size distribution histogram, SEM, optical and fluorescence images of CVD grown WS_2 monolayer flakes on hBN; optical, fluorescence and PL images of exfoliated WS_2 monolayer flake on SiO_2/Si; PL images of CVD grown WS_2 monolayer flakes on hBN under different magnetic fields; valley Zeeman splitting plots of selected area of CVD grown WS_2 monolayer flakes on hBN; statistic size distribution histogram, Raman spectrum, SEM, AFM and optical images of CVD grown MoS_2 monolayer flakes on hBN; PL images of CVD grown MoS_2 monolayer flakes on hBN under different magnetic fields) is available in the online version of this article at https://doi.org/10.1007/s12274-018-2142-5.

References

[1] Mak, K. F.; Shan, J. Photonics and optoelectronics of 2D semiconductor transition metal dichalcogenides. *Nat. Photonics* **2016**, *10*, 216–226.

[2] Duan, X. D.; Wang, C.; Pan, A. L.; Yu, R. Q.; Duan, X. F. Two-dimensional transition metal dichalcogenides as atomically thin semiconductors: Opportunities and challenges. *Chem. Soc. Rev.* **2015**, *44*, 8859–8876.

[3] Yu, H. Y.; Cui, X. D.; Xu, X. D.; Yao, W. Valley excitons in two-dimensional semiconductors. *Natl. Sci. Rev.* **2015**, *2*, 57–70.

[4] Peng, B.; Ang, P. K.; Loh, K. P. Two-dimensional dichalcogenides for light-harvesting applications. *Nano Today* **2015**, *10*, 128–137.

[5] Withers, F.; Del Pozo-Zamudio, O.; Mishchenko, A.; Rooney, A. P.; Gholinia, A.; Watanabe, K.; Taniguchi, T.; Haigh, S. J.; Geim, A. K.; Tartakovskii, A. I. et al. Light-emitting diodes by band-structure engineering in van der Waals heterostructures. *Nat. Mater.* **2015**, *14*, 301–306.

[6] Wu, S. F.; Buckley, S.; Schaibley, J. R.; Feng, L. F.; Yan, J. Q.; Mandrus, D. G.; Hatami, F.; Yao, W.; Vučković, J.; Majumdar, A. et al. Monolayer semiconductor nanocavity lasers with ultralow thresholds. *Nature* **2015**, *520*, 69–72.

[7] Ye, Y.; Wong, Z. J.; Lu, X. F.; Ni, X. J.; Zhu, H. Y.; Chen, X. H.; Wang, Y.; Zhang, X. Monolayer excitonic laser. *Nat. Photonics* **2015**, *9*, 733–737.

[8] Zhang, Y. J.; Oka, T.; Suzuki, R.; Ye, J. T.; Iwasa, Y. Electrically switchable chiral light-emitting transistor. *Science* **2014**, *344*, 725–728.

[9] Ross, J. S.; Klement, P.; Jones, A. M.; Ghimire, N. J.; Yan, J. Q.; Mandrus, D. G.; Taniguchi, T.; Watanabe, K.; Kitamura, K.; Yao, W. et al. Electrically tunable excitonic light-emitting diodes based on monolayer WSe_2 p–n junctions. *Nat. Nanotechnol.* **2014**, *9*, 268–272.

[10] Eda, G.; Maier, S. A. Two-dimensional crystals: Managing light for optoelectronics. *ACS Nano* **2013**, *7*, 5660–5665.

[11] Wang, Q. H.; Kalantar-Zadeh, K.; Kis, A.; Coleman, J. N.; Strano, M. S. Electronics and optoelectronics of two-dimensional transition metal dichalcogenides. *Nat. Nanotechnol.* **2012**, *7*, 699–712.

[12] Zeng, H. L.; Cui, X. D. An optical spectroscopic study on two-dimensional group-VI transition metal dichalcogenides. *Chem. Soc. Rev.* **2015**, *44*, 2629–2642.

[13] Cong, C. X.; Shang, J. Z.; Wang, Y. L.; Yu, T. Optical properties of 2D semiconductor WS_2. *Adv. Opt. Mater.* **2018**, *6*, 1700767.

[14] Shang, J. Z.; Cong, C. X.; Wang, Z. L.; Peimyoo, N.; Wu, L. S.; Zou, C. J.; Chen, Y.; Chin, X. Y.; Wang, J. P.; Soci, C.

et al. Room-temperature 2D semiconductor activated vertical-cavity surface-emitting lasers. *Nat. Commun.* **2017**, *8*, 543.

[15] Lee, Y. H.; Zhang, X. Q.; Zhang, W. J.; Chang, M. T.; Lin, C. T.; Chang, K. D.; Yu, Y. C.; Wang, J. T. W.; Chang, C. S.; Li, L. J. et al. Synthesis of large-area MoS_2 atomic layers with chemical vapor deposition. *Adv. Mater.* **2012**, *24*, 2320–2325.

[16] Gong, Y. J.; Ye, G. L.; Lei, S. D.; Shi, G.; He, Y. M.; Lin, J. H.; Zhang, X.; Vajtai, R.; Pantelides, S. T.; Zhou, W. et al. Synthesis of millimeter-scale transition metal dichalcogenides single crystals. *Adv. Funct. Mater.* **2016**, *26*, 2009–2015.

[17] Cong, C. X.; Shang, J. Z.; Wu, X.; Cao, B. C.; Peimyoo, N.; Qiu, C. Y.; Sun, L. T.; Yu, T. Synthesis and optical properties of large-area single-crystalline 2D semiconductor WS_2 monolayer from chemical vapor deposition. *Adv. Opt. Mater.* **2014**, *2*, 131–136.

[18] van der Zande, A. M.; Huang, P. Y.; Chenet, D. A.; Berkelbach, T. C.; You, Y.; Lee, G. H.; Heinz, T. F.; Reichman, D. R.; Muller, D. A.; Hone, J. C. Grains and grain boundaries in highly crystalline monolayer molybdenum disulphide. *Nat. Mater.* **2013**, *12*, 554–561.

[19] Zhang, Y.; Zhang, Y. F.; Ji, Q. Q.; Ju, J.; Yuan, H. T.; Shi, J. P.; Gao, T.; Ma, D. L.; Liu, M. X.; Chen, Y. B. et al. Controlled growth of high-quality monolayer WS_2 layers on sapphire and imaging its grain boundary. *ACS Nano* **2013**, *7*, 8963–8971.

[20] Gao, Y.; Liu, Z. B.; Sun, D. M.; Huang, L.; Ma, L. P.; Yin, L. C.; Ma, T.; Zhang, Z. Y.; Ma, X. L.; Peng, L. M. et al. Large-area synthesis of high-quality and uniform monolayer WS_2 on reusable Au foils. *Nat. Commun.* **2015**, *6*, 8569.

[21] Yu, H.; Liao, M. Z.; Zhao, W. J.; Liu, G. D.; Zhou, X. J.; Wei, Z.; Xu, X. Z.; Liu, K. H.; Hu, Z. H.; Deng, K. et al. Wafer-scale growth and transfer of highly-oriented monolayer MoS_2 continuous films. *ACS Nano* **2017**, *11*, 12001–12007.

[22] Zhao, W. F.; Yu, H.; Liao, M. Z.; Zhang, L.; Zou, S. Z.; Yu, H. J.; He, C. J.; Zhang, J. Y.; Zhang, G. Y.; Lin, X. C. Large area growth of monolayer MoS_2 film on quartz and its use as a saturable absorber in laser mode-locking. *Semicond. Sci. Technol.* **2017**, *32*, 025013.

[23] Ji, Q. Q.; Zhang, Y. F.; Gao, T.; Zhang, Y.; Ma, D. L.; Liu, M. X.; Chen, Y. B.; Qiao, X. F.; Tan, P. H.; Kan, M. et al. Epitaxial monolayer MoS_2 on mica with novel photoluminescence. *Nano Lett.* **2013**, *13*, 3870–3877.

[24] Okada, M.; Sawazaki, T.; Watanabe, K.; Taniguch, T.; Hibino, H.; Shinohara, H.; Kitaura, R. Direct chemical vapor deposition growth of WS_2 atomic layers on hexagonal boron nitride. *ACS Nano* **2014**, *8*, 8273–8277.

[25] Kobayashi, Y.; Sasaki, S.; Mori, S.; Hibino, H.; Liu, Z.; Watanabe, K.; Taniguchi, T.; Suenaga, K.; Maniwa, Y.; Miyata, Y. Growth and optical properties of high-quality monolayer WS_2 on graphite. *ACS Nano* **2015**, *9*, 4056–4063.

[26] Cadiz, F.; Courtade, E.; Robert, C.; Wang, G.; Shen, Y.; Cai, H.; Taniguchi, T.; Watanabe, K.; Carrere, H.; Lagarde, D. et al. Excitonic linewidth approaching the homogeneous limit in MoS_2-based van der Waals heterostructures. *Phys. Rev. X* **2017**, *7*, 021026.

[27] Cui, X.; Lee, G. H.; Kim, Y. D.; Arefe, G.; Huang, P. Y.; Lee, C. H.; Chenet, D. A.; Zhang, X.; Wang, L.; Ye, F. et al. Multi-terminal transport measurements of MoS_2 using a van der Waals heterostructure device platform. *Nat. Nanotechnol.* **2015**, *10*, 534–540.

[28] Jin, C. H.; Kim, J.; Suh, J.; Shi, Z. W.; Chen, B.; Fan, X.; Kam, M.; Watanabe, K.; Taniguchi, T.; Tongay, S. et al. Interlayer electron-phonon coupling in WSe_2/hBN heterostructures. *Nat. Phys.* **2017**, *13*, 127–131.

[29] Wang, Z. F.; Shan, J.; Mak, K. F. Valley- and spin-polarized Landau levels in monolayer WSe_2. *Nat. Nanotechnol.* **2016**, *12*, 144–149.

[30] Ajayi, O. A.; Ardelean, J. V.; Shepard, G. D.; Wang, J.; Antony, A.; Taniguchi, T.; Watanabe, K.; Heinz, T. F.; Strauf, S.; Zhu, X. Y. et al. Approaching the intrinsic photoluminescence linewidth in transition metal dichalcogenide monolayers. *2D Mater.* **2017**, *4*, 031011.

[31] Manca, M.; Glazov, M. M.; Robert, C.; Cadiz, F.; Taniguchi, T.; Watanabe, K.; Courtade, E.; Amand, T.; Renucci, P.; Marie, X. et al. Enabling valley selective exciton scattering in monolayer WSe_2 through upconversion. *Nat. Commun.* **2017**, *8*, 14927.

[32] Chow, C. M.; Yu, H. Y.; Jones, A. M.; Yan, J. Q.; Mandrus, D. G.; Taniguchi, T.; Watanabe, K.; Yao, W.; Xu, X. D. Unusual exciton-phonon interactions at van der Waals engineered interfaces. *Nano Lett.* **2017**, *17*, 1194–1199.

[33] Yu, H.; Yang, Z. Z.; Du, L. J.; Zhang, J.; Shi, J.; Chen, W.; Chen, P.; Liao, M. Z.; Zhao, J.; Meng, J. L. et al. Precisely aligned monolayer MoS_2 epitaxially grown on h-BN basal plane. *Small* **2017**, *13*, 1603005.

[34] Yan, A. M.; Velasco, J.; Kahn, S.; Watanabe, K.; Taniguchi, T.; Wang, F.; Crommie, M. F.; Zettl, A. Direct growth of single- and few-layer MoS_2 on h-BN with preferred relative rotation angles. *Nano Lett.* **2015**, *15*, 6324–6331.

[35] Okada, M.; Miyauchi, Y.; Matsuda, K.; Taniguchi, T.; Watanabe, K.; Shinohara, H.; Kitaura, R. Observation of biexcitonic emission at extremely low power density in tungsten disulfide atomic layers grown on hexagonal boron nitride. *Sci. Rep.* **2017**, *7*, 322.

[36] MacNeill, D.; Heikes, C.; Mak, K. F.; Anderson, Z.; Kormányos, A.; Zólyomi, V.; Park, J.; Ralph, D. C. Breaking of valley degeneracy by magnetic field in monolayer $MoSe_2$. *Phys. Rev. Lett.* **2015**, *114*, 037401.

[37] Aivazian, G.; Gong, Z. R.; Jones, A. M.; Chu, R. L.; Yan, J.; Mandrus, D. G.; Zhang, C. W.; Cobden, D.; Yao, W.; Xu, X. Magnetic control of valley pseudospin in monolayer WSe_2. *Nat. Phys.* **2015**, *11*, 148–152.

[38] Li, Y. L.; Ludwig, J.; Low, T.; Chernikov, A.; Cui, X.; Arefe, G.; Kim, Y. D.; van der Zande, A. M.; Rigosi, A.; Hill, H. M. et al. Valley splitting and polarization by the Zeeman effect in monolayer $MoSe_2$. *Phys. Rev. Lett.* **2014**, *113*, 266804.

[39] Srivastava, A.; Sidler, M.; Allain, A. V.; Lembke, D. S.; Kis, A.; Imamoğlu, A. Valley Zeeman effect in elementary optical excitations of monolayer WSe_2. *Nat. Phys.* **2015**, *11*, 141–147.

[40] Wang, G.; Bouet, L.; Lagarde, D.; Vidal, M.; Balocchi, A.; Amand, T.; Marie, X.; Urbaszek, B. Valley dynamics probed through charged and neutral exciton emission in monolayer WSe_2. *Phys. Rev. B* **2014**, *90*, 075413.

[41] Zhu, C. R.; Zhang, K.; Glazov, M.; Urbaszek, B.; Amand, T.; Ji, Z. W.; Liu, B. L.; Marie, X. Exciton valley dynamics probed by Kerr rotation in WSe_2 monolayers. *Phys. Rev. B* **2014**, *90*, 161302.

[42] Shang, J. Z.; Shen, X. N.; Cong, C. X.; Peimyoo, N.; Cao, B. C.; Eginligil, M.; Yu, T. Observation of excitonic fine structure in a 2D transition-metal dichalcogenide semiconductor. *ACS Nano* **2015**, *9*, 647–655.

[43] Shang, J. Z.; Cong, C. X.; Shen, X. N.; Yang, W. H.; Zou, C. J.; Peimyoo, N.; Cao, B. C.; Eginligil, M.; Lin, W.; Huang, W. et al. Revealing electronic nature of broad bound exciton bands in two-dimensional semiconducting WS_2 and MoS_2. *Phys. Rev. Mater.* **2017**, *1*, 074001.

[44] Christopher, J. W.; Goldberg, B. B.; Swan, A. K. Long tailed trions in monolayer MoS_2: Temperature dependent asymmetry and resulting red-shift of trion photoluminescence spectra. *Sci. Rep.* **2017**, *7*, 14062.

[45] Berkdemir, A.; Gutiérrez, H. R.; Botello-Méndez, A. R.; Perea-López, N.; Elías, A. L.; Chia, C. I.; Wang, B.; Crespi, V. H.; López-Urías, F.; Charlier, J. C. et al. Identification of individual and few layers of WS_2 using Raman spectroscopy. *Sci. Rep.* **2013**, *3*, 1755.

[46] Desai, S. B.; Seol, G.; Kang, J. S.; Fang, H.; Battaglia, C.; Kapadia, R.; Ager, J. W.; Guo, J.; Javey, A. Strain-induced indirect to direct bandgap transition in multilayer WSe_2. *Nano Lett.* **2014**, *14*, 4592–4597.

[47] Lin, Y. X.; Ling, X.; Yu, L. L.; Huang, S. X.; Hsu, A. L.; Lee, Y. H.; Kong, J.; Dresselhaus, M. S.; Palacios, T. Dielectric screening of excitons and trions in single-layer MoS_2. *Nano Lett.* **2014**, *14*, 5569–5576.

[48] Chernikov, A.; Berkelbach, T. C.; Hill, H. M.; Rigosi, A.; Li, Y. L.; Aslan, O. B.; Reichman, D. R.; Hybertsen, M. S.; Heinz, T. F. Exciton binding energy and nonhydrogenic Rydberg series in monolayer WS_2. *Phys. Rev. Lett.* **2014**, *113*, 076802.

[49] Zhu, B. R.; Chen, X.; Cui, X. D. Exciton binding energy of monolayer WS_2. *Sci. Rep.* **2015**, *5*, 9218.

[50] Mitioglu, A. A.; Plochocka, P.; Jadczak, J. N.; Escoffier, W.; Rikken, G. L. J. A.; Kulyuk, L.; Maude, D. K. Optical manipulation of the exciton charge state in single-layer tungsten disulfide. *Phys. Rev. B* **2013**, *88*, 245403.

[51] Szyniszewski, M.; Mostaani, E.; Drummond, N. D.; Fal'ko, V. I. Binding energies of trions and biexcitons in two-dimensional semiconductors from diffusion quantum Monte Carlo calculations. *Phys. Rev. B* **2017**, *95*, 081301.

[52] Zhang, D. K.; Kidd, D. W.; Varga, K. Excited biexcitons in transition metal dichalcogenides. *Nano Lett.* **2015**, *15*, 7002–7005.